(Received 5 December 2024, Accepted 18 December 2024, Scheduled 19 December 2024)

Large Dynamic Range Slope-Assisted BOTDA Based on Unbalanced Frequency-Shifted Double Sidebands Detection

Zijian Xiong[1], Shengnan Wu[1, 2, 3, *], and Sailing He[1, 2, 3, *]

[1] *National Engineering Research Center for Optical Instruments, College of Optical Science and Engineering Zhejiang University, Hangzhou 310058, China*
[2] *Ningbo Research Institute, Zhejiang University, Ningbo 315100, China*
[3] *School of Information Science and Engineering, NingboTech University, Ningbo 315100, China*

ABSTRACT: To increase the dynamic detection range of slope-assisted Brillouin optical time-domain analysis (SA-BOTDA) system, we propose a configuration using unbalanced frequency-shifted Stokes and anti-Stokes sidebands as continuous probe light simultaneously to expand the region of effective stimulated Brillouin scattering (SBS) spectrum existed in the frequency domain. The proposed scheme fully utilizes the gain, loss and corresponding phase spectra of the unbalanced double sidebands, constructs linear regions by specific data processing methods and is independent of the pump power. We employ a scheme of agile switching between two frequencies to broaden the linear region at the cost of detection speed. The dynamic detection range of the proposed system can be over 180 MHz, with a spatial resolution of 3.5 m and 500 MHz sampling rate for vibration detection.

1. INTRODUCTION

Compared with traditional electronic sensors, optical sensors have many advantages, such as immune to electromagnetic interference corrosion resistance, small size, light weight, and suitable for extreme environments [1–4]. Distributed fiber sensors are one of the most important parts in the field of fiber optic sensing [5–7], characterized by fully utilizing the scattered signals of scattering units at any position along the entire optical fiber. Therefore, fiber can serve as both transmission channel and sensor itself. Among them, Brillouin optical time-domain analysis (BOTDA) is a kind of distributed fiber sensing technology based on stimulated Brillouin scattering (SBS), has excellent advantages such as long sensing distance, high signal-to-noise ratio, high spatial resolution, and the ability to sense both temperature and strain information. It is widely used in building security, oil, gas and water pipelines, and railway traffic detection [8–12]. For a traditional BOTDA system, the frequency scanning procedure needs dozens of frequency-shift times, and to solve polarization fading problem, over hundreds of average times is required under the operation of polarization scrambler, which limits the demodulation speed of BOTDA system.

Some groups have proposed frequency-agile Brillouin optical time-domain analysis technique (F-BOTDA) method, which utilizes ns level frequency switching by arbitrary waveform generators (AWG) to greatly reduce the time required for commonly used frequency switching methods [7]. However, to improve the dynamic detection range and ensure detection accuracy, increasing frequency switching times is necessary, which will affect the dynamic bandwidth. Sweep free BOTDA (SF-BOTDA) launches probe light or pump pulse modulated by frequency comb into the sensing fiber to avoid the scanning process [13–15]. However, this method had a trade-off between spatial resolution and frequency resolution. The optical chirp chain BOTDA (OCC-BOTDA) modulates the continuous detection light into a chirped state, ensuring m-level spatial resolution and no need for scanning [16–18]. However, the scheme requires high frequency source performance, and due to the Brillouin phonon relaxation effect, the resulting signal undergoes deformation compared to the Lorentz curve of the Brillouin gain/loss spectrum (BGS/BLS), requiring subsequent data processing.

In the past decade, various slope assisted BOTDA (SA-BOTDA) schemes have been proposed, which basically utilizes a single frequency to lock the slope of the SBS gain spectrum for dynamic detection, or dual-slope/multi-slope BOTDA with alternating frequency, but the range is typically below 40 MHz under single frequency [19–21]. Some schemes propose using specially modulated multi-frequency pump light to construct large linear slope of the SBS gain spectrum or phase spectrum above 100 MHz, but the results of this scheme are greatly affected by pump power [19, 22–24]. By using the ratio of Brillouin phase shift spectrum and Brillouin gain spectrum, a pump power independent linear region is constructed [25–27]. However, due to the interference of spectrum and signal-to-noise ratio (SNR) limited, the maximum range of the linear region can only be around 100 MHz. Due to the frequency crosstalk between the signal light and the reference light, the frequency interval between the two lights is often required to be three times more than width of linear region. For larger dynamic linear detection range, a data acquisition card (DAQ) or a photodetector (PD) with a bandwidth of 1 GHz or more is often required, which increases the cost.

* Corresponding authors: Shengnan Wu (wushengnan@zju.edu.cn); Sailing He (sailing@zju.edu.cn).

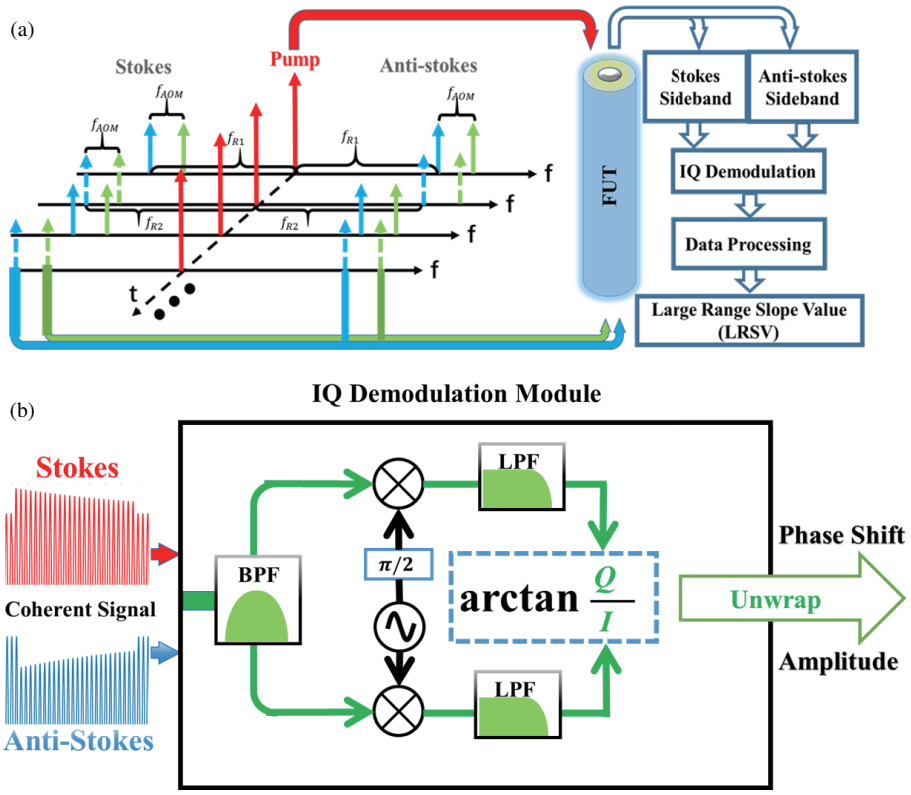

FIGURE 1. Sketch map and simulation of slope-assisted BOTDA system based on unbalanced double sidebands detection. (a) Illustration of the proposed technique; (b) Schematic diagram of IQ demodulation process.

In this article, we propose a scheme to construct double sideband asymmetric SBS spectrum through frequency blue shift (100 MHz). Instead of using the large frequency interval between reference and signal light to suppress crosstalk and ensure the quality of the linear region, we use the unbalanced gain/loss spectrum and phase shift spectrum combined with agile switching between two frequencies and polarization compensation technology to build large dynamic linear region over 180 MHz. Using the large frequency interval between reference and signal light suppresses crosstalk and ensures the quality of the linear region. The scheme has been experimentally verified showing that a spatial resolution of 3.5 m can be achieved in single-mode optical fibers over 850 m, and a time-domain signal with an amplitude of approximately and a frequency of about 27.5 Hz has been successfully detected through motor vibration tests. (Limited by engine vibration rate and amplitude).

2. PRINCIPLE

The schematic diagram of the proposed method is shown in Fig. 1(a). The system emits a sequence of pump pulses at certain repetition rate from one end. When the number of sequences is odd, the frequency interval between the dual sideband probe light (blue) and the pump light frequency is f_{R1}. At the same time, both sidebands have reference light (green) of the same power whose frequency is f_{AOM} higher than probe light. The reference light and probe light are injected from the other end of the fiber under test (FUT), opposite to the direction of the pump pulse. When the pulse sequence is even, the interval between them is f_{R2}, and other conditions are kept the same. After interacting with the pump pulse light, the expression of signal light E_{sig} can be obtained as shown:

$$\begin{aligned} E_{sig}(z) &= E_{SS}(z)+E_{SR}(z)+E_{ASS}(z)+E_{ASR}(z) \\ &= E_0(z)\left\{\begin{array}{l} e^{g(v_{SS},z)+j[2\pi v_{SS}t+\varphi(v_{SS},z)-kz]} \\ +e^{g(v_{SR},z)+j[2\pi v_{SR}t+\varphi(v_{SR},z)-kz]} \\ +e^{-g(v_{ASS},z)+j[2\pi v_{ASS}t-\varphi(v_{ASS},z)-kz]} \\ +e^{-g(v_{ASR},z)+j[2\pi v_{ASR}t-\varphi(v_{ASR},z)-kz]} \end{array}\right\} \end{aligned} \quad (1)$$

where E_{SS}, E_{SR}, E_{ASS}, and E_{ASR} are the amplitude of probe light and reference light in Stokes sideband and Anti-Stokes sideband respectively. v_{SS}, v_{SR}, v_{ASS}, and v_{ASR} are their frequencies respectively. E_0 is the initial amplitude without SBS, while $g(v,z)$ and $\varphi(v,z)$ are gain spectrum and phase shift spectrum of SBS, which can be expressed as:

$$\left\{\begin{array}{l} g(v) \propto \eta |E_p|^2 \dfrac{\Delta v_B^2}{4(v-v_B)^2+\Delta v_B^2} \\ \varphi(v) \propto \eta |E_p|^2 \dfrac{2\Delta v_B (v-v_B)}{4(v-v_B)^2+\Delta v_B^2} \end{array}\right. \quad (2)$$

where η is the polarization index and indicates the inner product of Jones vectors for pump light and probe light; E_p is the amplitude of pump light; v_B is the central Brillouin frequency shift (BFS); and Δv_B is the linewidth of BGS.

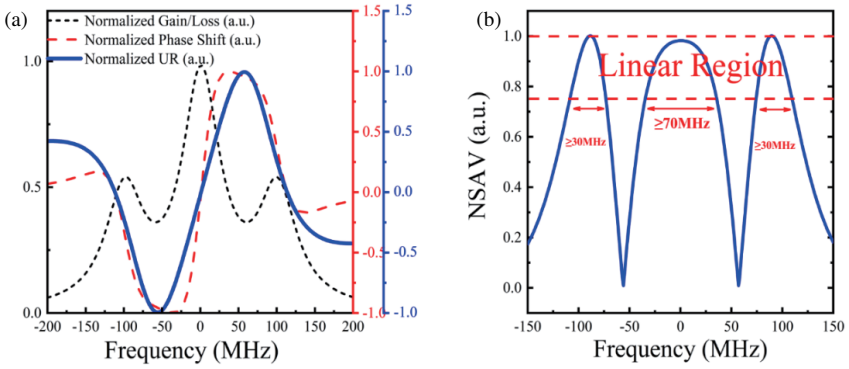

FIGURE 2. (a) Simulation of normalized gain/loss, phase shift and *UR* spectrum of the proposed scheme near the central Brillouin frequency shift; (b) Simulation of normalized slope absolute value (*NSAV*) of *UR* spectra.

Due to the limited bandwidth of photodetector (PD) and DAQ, only the beat signals of the probe and reference light in the same sideband can be detected. Two narrow optical band-pass filters are used to separate the two sidebands and the expressions of the received dual-sideband signals after PD are:

$$\begin{cases} I_S(v,z) = 2R_D E_{SS} E_{SR}(1 + g(v,z) \\ \quad + g(v + f_{AOM}, z)) \cdot \cos(2\pi f_{AOM} t + \varphi(v,z) \\ \quad - \varphi(v + f_{AOM}, z)) \\ I_{AS}(v,z) = 2R_D E_{ASS} E_{ASR}(1 - g(v,z) \\ \quad - g(v - f_{AOM}, z)) \cdot \cos(2\pi f_{AOM} t + \varphi(v,z) \\ \quad - \varphi(v - f_{AOM}, z)) \end{cases} \tag{3}$$

where R_D is the responsivity of PD.

IQ demodulation is a common method used for demodulating and analyzing signals. IQ represents two key attributes of a signal: I (In Phase) and Q (Quadrature). By demodulating the I and Q components of the signal, the phase and amplitude information of the signal can be obtained, thereby achieving signal demodulation and analysis. Using IQ demodulation as shown in Fig. 1(b), the gain spectrum and phase shift spectrum of both Stokes and Anti-stokes sidebands can be obtained separately. The low frequency component of the interference signal is received by the photodetector and converted into the corresponding RF signal as shown in Eq. (3). After passing through a band-pass digital filter centered at f_{AOM}, the signal processing is divided into two paths. One path called I path mixed with a cosine signal of frequency f_{AOM}, and the mixed signal is filtered by a low-pass filter to obtain the "I" value. Similarly, the other path is also mixed with signal of frequency f_{AOM}, and the cosine wave contains additional $\pi/2$ phase shift compared to the other path, which is used as Q path. The mixed result passes through another low-pass filter to get the "Q" value. Through a subsequent arctangent operation and unwrapping processing, the amplitude and phase information of coherent signals can be fully obtained. By adding the unbalanced phase shift spectra and subtracting of gain/loss spectra in Stokes and anti-Stokes sideband, effective SBS spectra range get larger, represented as g_U and φ_U respectively.

$$\begin{cases} g_U(v,z) = 2g(v,z) + g(v + f_{AOM}, z) + g(v - f_{AOM}, z) \\ \varphi_U(v,z) = 2\varphi(v,z) - \varphi(v + f_{AOM}, z) - \varphi(v - f_{AOM}, z) \end{cases} \tag{4}$$

The unbalanced ratio (UR) of phase shift and gain spectra in this scheme can be expressed as φ_U/g_U. Due to the linear characteristic of φ/g, it can be inferred that there are three linear regions at the frequency of v_B and $v_B \pm f_{AOM} in UR$. Additionally, if the observed region is close to Brillouin frequency shift v_B, due to the large weight proportion in both the gain spectrum and phase spectrum, there will be a larger linear region. Although containing other frequency components' crosstalk, effective linear region also exists at other two parts (around $v \pm f_{AOM}$), according to the measured spectrum of the fiber at the test position. Simulation is operated for normalized g_U, φ_U, UR and normalized slope absolute value (NSAV) of UR in Figs. 2(a) and 2(b). Assuming that the slope fluctuation limit is 25% for linear condition, three linear regions can be obtained, with widths of at least 30 MHz, 70 MHz, and 30 MHz. To fully utilize multiple linear regions to synthesize a larger linear region, we employ a scheme of agile switching (with the repetition rate of the pulse train) between the two frequencies (hereafter referred as dual-frequency agile-switching), sacrificing half of detection bandwidth for a larger linear dynamic range. It is possible to distinguish each linear region by comparing UR at two frequencies and achieve expected effect through appropriate computational processing. In addition, the influence of pump light power can be suppressed by ratio relationship.

3. EXPERIMENTAL SETUP

The experimental setup for the unbalanced double sideband slope-assisted BOTDA is shown in Fig. 3, and a narrow linewidth laser (NLL, 1550.21 nm wavelength, $\sim$ 4 kHz linewidth) is used as the light source. The laser from NLL is divided into two branches by a 3 dB coupler. The pump pulses are generated in the upper propagation path. On the upper branch, the pump light wave is pulsed by semiconductor optical amplifier (SOA) with 35 ns pulse width and

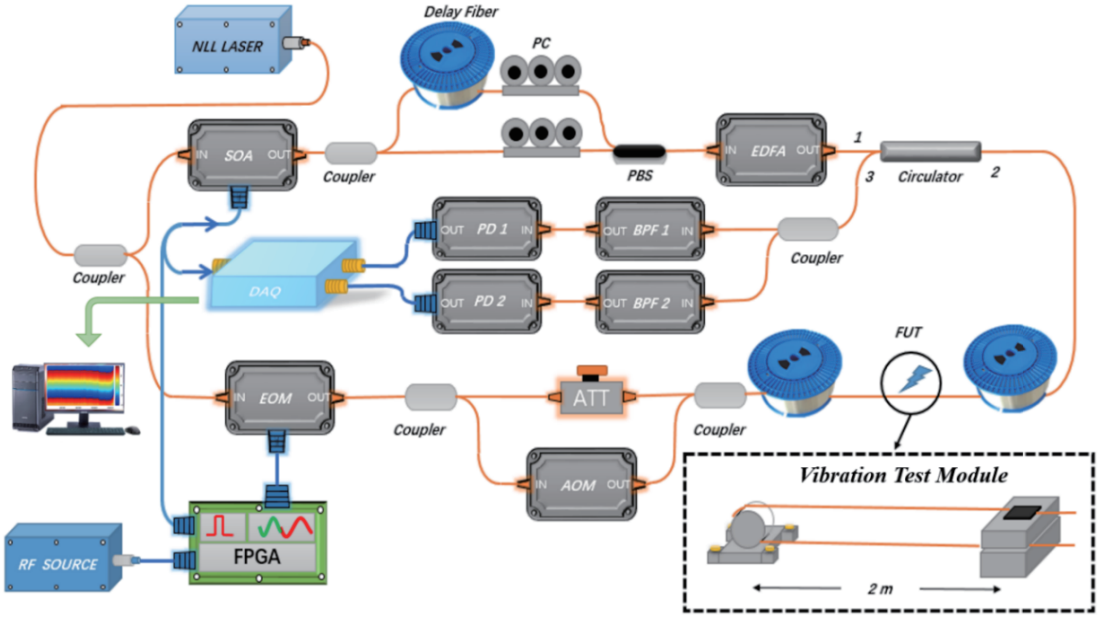

FIGURE 3. Experimental setup. NLL, narrow linewidth laser; SOA, semiconductor optical amplifier; PC, polarization controller; EDFA, erbium-doped fiber amplifier; FUT, fiber under test; EOM, electro-optic modulator; RF, radio frequency; AOM, acousto-optic modulator; ATT, attenuator; BPF, (optical) band-pass filter; PD, photodetector; DAQ, data acquisition card; FPGA, field programmable gate array.

5 kHz repetition rate, which corresponds to a 3.5 m spatial resolution. The polarization fading of SBS can be suppressed by generating two orthogonal pulses with a certain time interval through subsequent polarization diversity structures, which utilizes delay fiber, polarization controllers (PC), and polarization beam coupler (PBC). The pulses are amplified by erbium-doped fiber amplifier (EDFA).

On the lower branch, an electro-optic modulator (EOM), an RF source and FPGA module are used to generate a dual-sideband optical signal with suppressed carrier signal light ($f_0 - f_{Ri},\ f_0 + f_{Ri}$) and make the agile switch between the two frequencies. Subsequently, an acousto-optic modulator (AOM) with a response center frequency of $f_{AOM} = 100$ MHz is used for frequency shift to generate reference light at $f_0 - f_{Ri} + f_{AOM}$ and $f_0 + f_{Ri} + f_{AOM}$. The optical power of each frequency is controlled to be around -2 dBm by attenuator (ATT) and then the probe light in different sidebands is launched into fiber under test (FUT). After passing through port 3 of circulator, the signal lights are separated by a coupler and only remain stokes sideband on one path and anti-stokes sideband on the other by optical band-pass filters (BPFs). The photodetectors (PDs) received the signals to CH1 and CH2 of the data acquisition card (DAQ) respectively. The FPGA module emits pulses to control the triggering of SOA and DAQ, while also controlling the switching time. The bandwidth of PD is 350 MHz and the maximum sampling rate of DAQ is 500 MHz. An 850 m SMF whose BFS is $\sim$ 10.820 GHz at 26° is employed in the experiment.

Agile dual-frequency switching. As shown in Fig. 4, we use the same set of electrically triggered pulses from FPGA to simultaneously trigger an optical pulse modulation module (to generate pump pulses) and a DAQ module (to acquire data). FPGA module gives control signals of fast switching between the high and low voltage levels, corresponding to the selection of RF switch in the two RF paths, to achieve agile switching between the two frequencies of f_{R1} and f_{R2} with a speed of about 150 ns. The voltage change of the "control signal" (green arrow) and the generation of the trigger pulse (red arrow) have a specific timing relationship (precisely programed in the FPGA module) so that a certain pump light pulse only interacts with the signal light modulated by the same frequency (f_{R1} or f_{R2}) and injected into FUT. For example, in the pump pulse train, odd numbered pump pulses only interact with the signal light modulated by f_{R1}, and even numbered pump pulses only interact with the signal light modulated by f_{R2}. This approach would double the amount of detection data, thereby halving the detection speed.

Timing relationship between trigger pulse and agile dual-frequency switching is shown in Fig. 4(b). Assuming that the trigger moment of an odd numbered pulse light is t_0 and the moment for frequency switching is t_f Point A represents the moment when the orthogonal pump pulse pair completely passes through the entire FUT. Point B represents the moment when the signal light modulated by f_{R2} passes through the fiber in the opposite direction. In order to ensure that the frequency of the signal light interacting with a certain pump pulse is consistent, the following timing conditions should be satisfied

$$t_0 + \frac{n\,(L + L_D)}{c} < t_f < t_0 + T - \left(\frac{nL}{c} + t_{RF}\right) \tag{5}$$

where n is the effective refractive index of SMF, and L and L_D are the total lengths of the FUT and delay fiber respectively. The switching time of the RF switch is represented as t_{RF}.

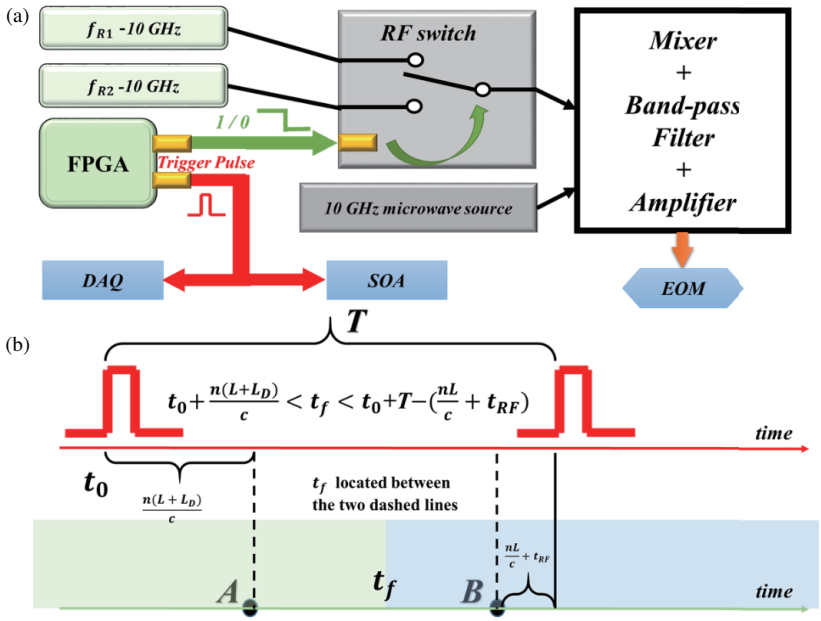

FIGURE 4. (a) Agile dual-frequency switching and the trigger module; (b) Timing relationship between the trigger pulse and agile dual-frequency switching.

The RF source is kept at 10 GHz, and the FPGA module is equipped with two tunable microwave frequency source channels, a frequency mixer, an RF filter, and an RF switch module. The frequency interval between the output signals of two channels can be set to 50 MHz, that is $f_{R2} = f_{R1} + 50$ MHz. The processed RF signal is loaded onto the EOM with a power of 16 dBm.

4. EXPERIMENTAL RESULT

4.1. Sensing Regions Judgment Method

We kept the position measured stable without disturbance, and at the same time, the computer controls the RF source to scan the frequency. The normalized mapping amplitude spectrum and phase shift spectrum of the two sidebands are recorded only when the number of pulse sequence is odd, i.e., only f_{R1} is active, which is shown in Fig. 5(a). The RF scanning range and step is 10.60 GHz–11.00 GHz and 2 MHz, respectively. We can also obtain the actual test diagrams of g_U and φ_U as shown in Fig. 5(b).

Under the action of f_{R1} and f_{R2} (which can be regarded as different frequency offset of Brillouin gain spectrum and phase spectrum), in order to detect the characteristics of the overall UR spectrum, the values of $UR1$ and $UR2$ can be obtained by scanning the frequency. To extend the length of linear region, $UR1$ and $UR2$ were combined, and their respective linear regions were used for stitching compensation to obtain LRSV with a larger dynamic range.

The measured UR and the linear fitting of the Large Range Slope Value (LRSV) within the range of 200 MHz are shown in Figs. 5(c) and (d), respectively, which is consistent with the simulation results. When the microwave frequencies loaded on EOM are f_{R1} and f_{R2}, UR is denoted as UR1 and UR2, respectively. Four linear regions are identified and synthesized into a linear region of up to 180 MHz through appropriate proportions and addition/subtraction operations, and the value is obtained for LRSV. The linear regions judgment method is shown below in Table 1. Through such an experiment we obtained the LRSV spectrum of the entire 850 m single-mode fiber through frequency scanning, further verifying the feasibility of the proposed scheme.

TABLE 1. Linear regions judgment method.

	Region 1	Region 2	Region 3	Region 4
$UR2-UR1$	>0	≤ 0	≤ 0	>0
$UR2+UR1$	≤ 0	≤ 0	>0	>0

4.2. Polarization Compensation

We used another 800 m optical fiber as test object to verify the polarization compensation effect of the proposed system. In the compensation scheme, two pump pulses with orthogonal polarization states are used to detect signal of each frame [28]. In the subsequent data processing, we sum the Brillouin gain spectra under two different polarization states to obtain the compensated three-dimensional Brillouin gain spectrum information as shown in Fig. 6(a). The polarization compensation effect in the proposed experimental configuration meets the actual detection requirements, and the phenomenon of polarization fading is effectively suppressed. Fig. 6(b) shows the gain-distance plot before and after polarization compensation when the fixed frequency shift is near the Brillouin center frequency, and the figure demonstrates the effectiveness of polarization compensation from the effect of overall and details of the first 20 m section of the fiber under test

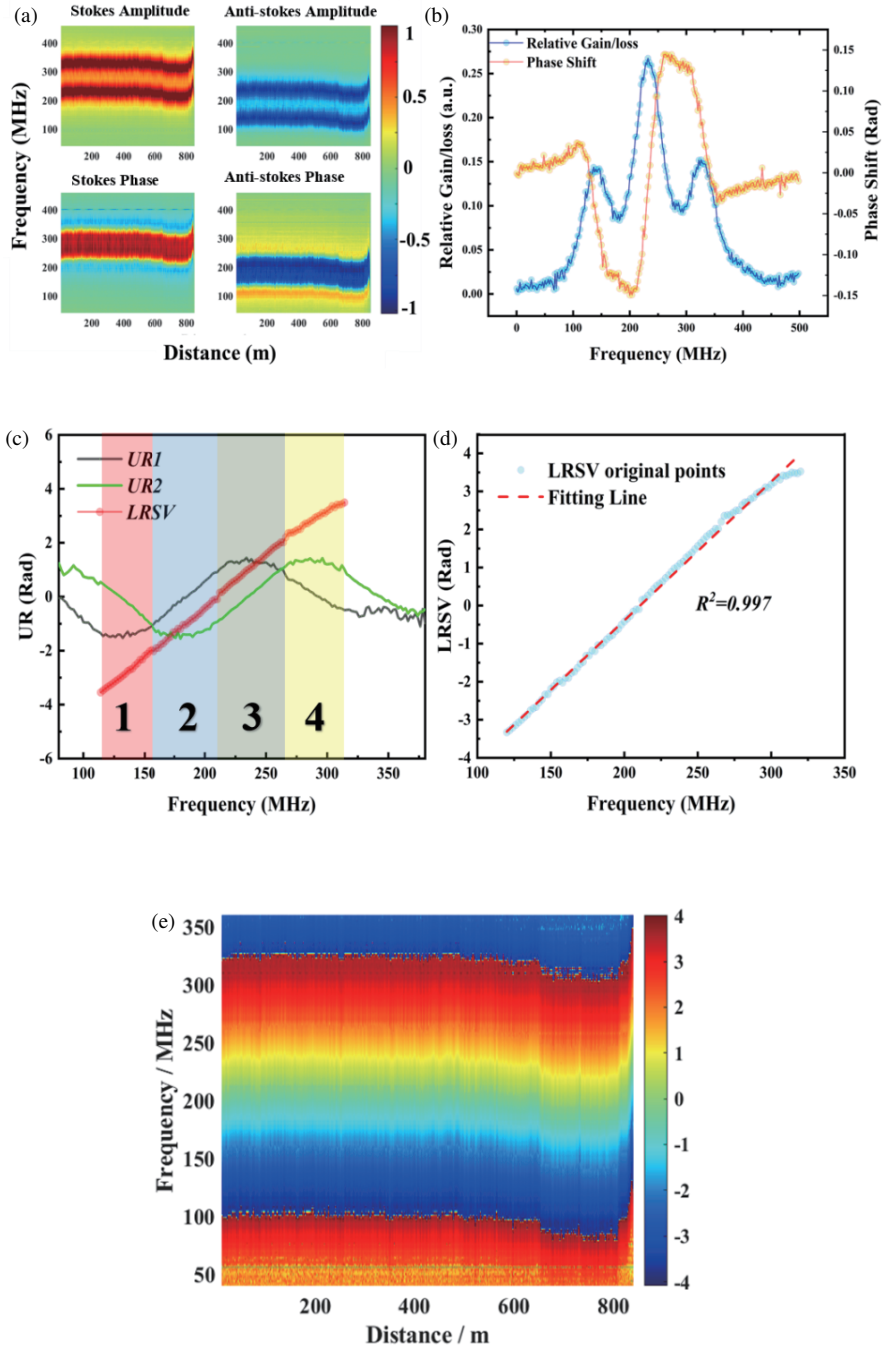

FIGURE 5. (a) Normalized mapping amplitude spectrum and phase shift spectrum of the two sidebands; (b) Actual test diagrams of g_U and φ_U; (c) UR1, UR2 and LRSV by frequency-scanning and (d) fitting line of LRSV; (e) Measured 3D LRSV spectrum diagram along an 850 m FUT.

4.3. Power-Independence of the System

To verify the power-independence of the proposed BOTDA system, we adjust the driving current (65 mA 70 mA and 75 mA) of EDFA after pulsed light to ensure its different amplification factors for the pump pulses. We measured the $\varphi_U(v)$ and LRSV(v) under three different states as shown in Fig. 7(a) and Fig. 7(b). Within an appropriate range, larger driving current means greater amplification factor for the pump pulses, which means that the Brillouin gain, loss, and Brillouin phase shift will increase proportionally. However, LRSV is proportional to the ratio of $\varphi_U(v)$ and $g_U(v)$, so the change in optical pump power causes the same proportional change to both $g_U(v, z)$ and $\varphi_U(v, z)$ values. Thus fluctuation caused by power fluctuations can be suppressed in data processing. The LRSV spectrum nearly maintains the same shape under different EDFA driving currents at different pump light power levels. As shown in Fig. 6(b), the SNR of the demodulated effective signal is greatly weakened when the pump power is not high enough such as "65 mA" curve in Fig. 7(b). Therefore, it is still necessary to ensure a certain level pump power for actual system testing.

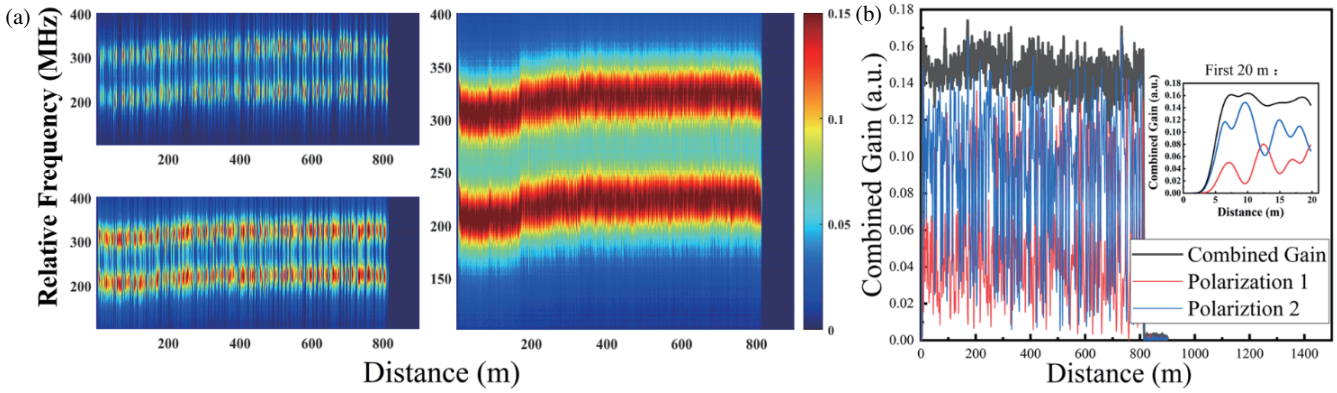

FIGURE 6. (a) 3D Brillouin gain spectra based on two orthogonal polarization states' pump pulse and result after compensation; (b) Gain-distance plot before and after polarization compensation.

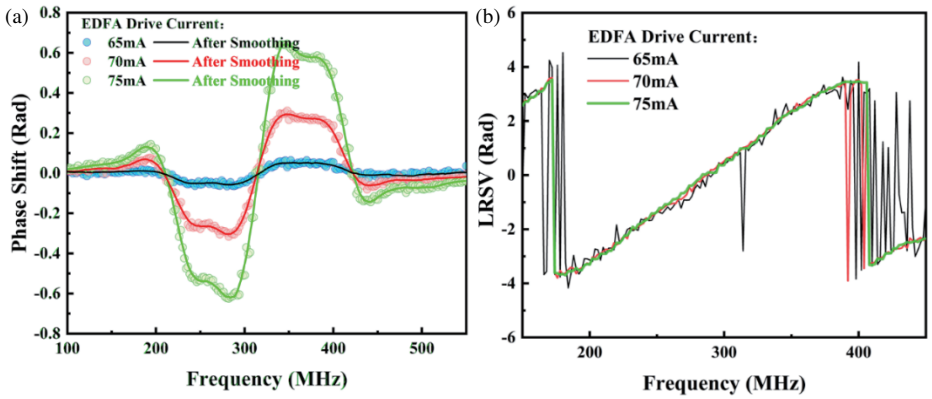

FIGURE 7. (a) Display of $\varphi_U(v)$ under different EDFA driving currents after pumping pulses; (b) Display of $LRSV(v)$ under different EDFA driving currents after pumping pulses.

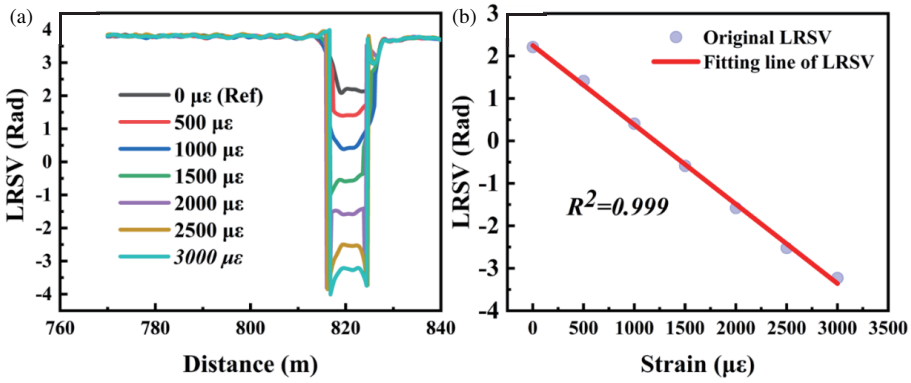

FIGURE 8. (a) Static strain test by 8m fiber section; (b) the linear fitting curve of Strain-LRSV.

4.4. Static and Dynamic Strain Sensing

To test the sensing performance of the unbalanced double sideband SA-BOTDA, a static strain test was executed. An 8 m fiber section is located at about 820 m, which is folded into two sections by circumference of a vibration motor with two ends tightly attached to micro-displacement stages. f_{R1} and f_{R2} are set as 10.880 GHz and 10.930 GHz, respectively, during the test, and a weak initial strain is applied to the 8 m fiber section (recorded as $0\mu\varepsilon$ as reference). One of the stages is gradually shifted to generate strain at step of $500\mu\varepsilon$ (4 mm/8 m), and the LRSV at any position along the fiber is recorded in Fig. 8(a). Strain up to $\sim 3000\mu\varepsilon$ can be successfully demodulated in this test. Fig. 8(b) shows the linear fitting curve of Strain-LRSV. The strain coefficient of FUT is measured to be $19.52\mu\varepsilon$/MHz.

To evaluate the long-term measurement error of the proposed method, we set a fixed strain state to the 4 m fiber section and select different average time. The strain fluctuation curves and minimum root mean square error (RMSE) within 100 ms

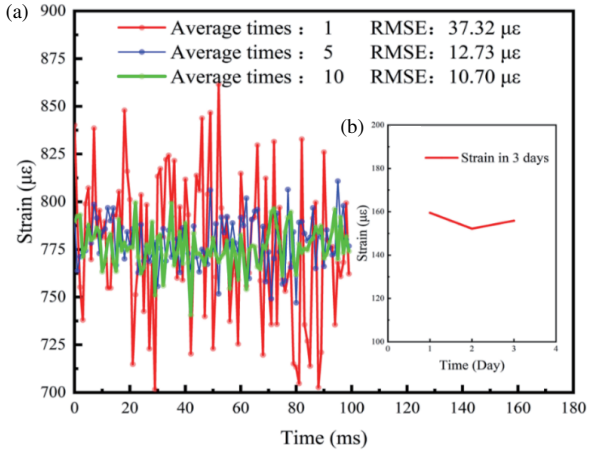

FIGURE 9. (a) Strain measurement error with different average times. (b) Inset: measured the same strain value once a day for three days.

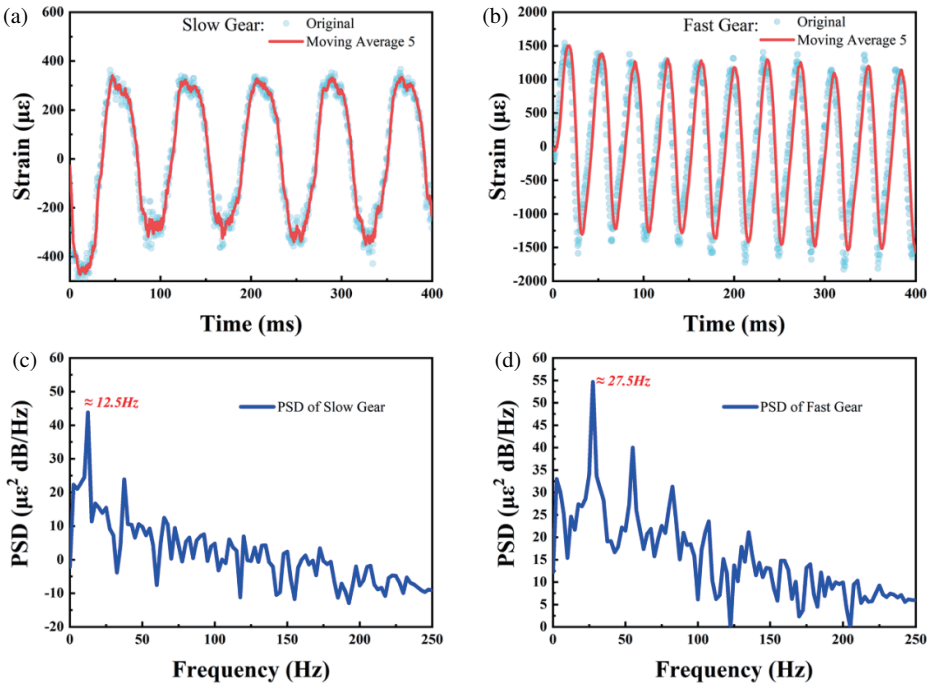

FIGURE 10. Vibration recovery from measured LRSV of the vibrated fiber change with time, when the motor is adjusted to (a) slow or (b) fast. (c) and (d) are their corresponding power spectral density.

are recorded in Fig. 9. The RMSE of the measured strain are 37.32$\mu\varepsilon$, 12.73$\mu\varepsilon$, and 10.70$\mu\varepsilon$ obtained by taking the average after repeated measurements for 1, 5, and 10 times, respectively. We kept the conditions and measured the same strain value once a day for three days, and the result is shown in Fig. 9. The variation of the measured strain is lower than 0.28% (ratio of the largest strain variation and dynamic range in 3 days), which indicates that the proposed system has great stability.

In the dynamic vibration test, a stretched 4 m fiber section was shocked periodically by an eccentric motor to induce vibration signal and cause dynamic strain along it. The pump pulse repetition rate is set to 5 kHz, and no average processing is set during this measurement process. By adjusting the knob, the eccentric wheel can be set to the fast and slow gears, respectively. The slow gear keeps lower vibration frequency and smaller amplitude, while the fast gear provides the opposite state. The demodulated vibration trace and power spectrum density (PSD) are shown in Fig. 10, which demonstrates the feasibility of large range dynamic detection for the vibration signal with amplitude of 2632$\mu\varepsilon$ and frequency up to 27.5 Hz.

4.5. Discussions

35 ns width pump pulses are used in proposed scheme, corresponding to a spatial resolution of 3.5 m. Tensile stress is applied to the fiber from 820 m to 825 m in the test, and its three-dimensional LRSV distribution map can be obtained as

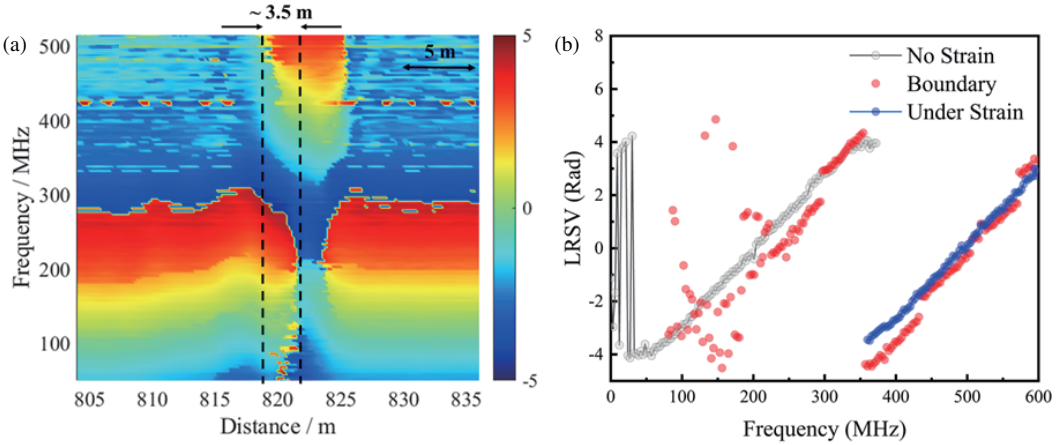

FIGURE 11. (a) 3D LRSV distribution map when tensile strain is applied to 820–825 m part of fiber under test; (b) LRSV diagram of strain-free region, stress-applied region, and their boundary region.

TABLE 2. Comparison of different slope-assisted BOTDA schemes.

	Dynamic Range/MHz	Pump Power-independence	Spatial Resolution/m	Frequency Segments Number	Sampling Rate Utilized/GHz
Single SA-BOTDA [29, 30]	35	No	3	1	Not mentioned
Double SA-BOTDA [21]	70	Yes	3	2	0.25
Multi SA-BOTDA [19]	241	Yes	~ 1	> 7	Not mentioned
Multi-frequency pump and probe [23]	100	No	Not mentioned	1	1
Single-BPGR [25]	8	Yes	2.5	1	> 1
Multi-BPGR [26]	254.3	Yes	3	6	5
Coherent Multi-SA-BOTDA [27]	180	Yes	2.5	1	4
The proposed scheme	**180**	**Yes**	3.5	**2**	**0.5**

shown in Fig. 11(a). Limited by spatial resolution, the spectra of $g_U(v)$ and $\varphi_U(v)$ exhibit overlapping shape at different positions in the edge regions between the strain and no strain regions, which can finally lead to discontinuous linear regions and slope value's changes in the demodulated LRSV during subsequent data processing as shown in Fig. 11(b). Unlike the gradual value changes at the edges for the traditional SA-BOTDA system, the demodulated results at boundary region sometimes show sudden change for the proposed scheme. It can explain the irregularity of edge position in Fig. 8(a) in the static strain test, but if the external environment of sensing location does not experience sudden significant changes (such as stress or temperature) within the spatial resolution limit, the detected results are basically normal

We show the comparative analysis between existing research and our proposed scheme. As illustrated in Table 2, our system's dynamic range surpasses 180 MHz through the agile switching of just two frequency components. Our scheme not only achieves this extensive dynamic range but also maintains pump power-independence, all at a modest sampling rate of 500 MHz which significantly cuts down on the cost of acquisition equipment. Although the system's spatial resolution could be theoretically enhanced, to preserve a high SNR and minimize average processing times, we have set the pump pulse width to 35 ns. Schemes based on single, double, or multiple slope-assisted BOTDA usually need a lower acquisition requirement due to direct detection for scattering intensity, but Brillouin phase information cannot be obtained by that approach which limits the improvement of system's performance.

5. CONCLUSION

A scheme to improve dynamic range based on unbalanced double sideband SA-BOTDA is proposed. By introducing unbalanced signal and reference light in both Stokes and Anti-stokes sideband simultaneously, the dynamic range can be extended to be over 180 MHz with the DAQ's sampling rate less than 500 MHz (more than $2f_{AOM}$ is enough). For a FUT of 850 m, the system can achieve a spatial resolution of 3.5 m, over 2.5 kHz sampling rate for vibration signal and is independent to pump power fluctuation. The proposed scheme provides a new idea for large-range dynamic detection of distributed optical fiber sensing, which can be applied for detecting temperature and hardening changes in extreme environments such as earthquake prevention and monitoring for the structural health of buildings.

ACKNOWLEDGEMENT

This work was supported partially by the Ningbo Science and Technology Project (2021Z030, 2021Z029, 2020Z077 and 2023Z179), the National Natural Science Foundation of China (62405275), the National Key Research and Development Program of China (2022YFC3601002), the Scientific Research Foundation for Talent Introduction of Zhejiang University's Ningbo Campus (20201203Z0180), and Ningbo Public Welfare Research Program Project (No. 2024Z234) The authors are also grateful to Dr. Julian Evans of Zhejiang University for helpful discussion.

REFERENCES

[1] Ai, Y., Z. Wang, Y. Liu, Y. Zheng, J. Wu, J. Zou, S. Zhang, P. Chen, and H. Peng, "Robust fiber strain sensor by designing coaxial coiling structure with mutual inductance effect," *Advanced Fiber Materials*, Vol. 6, No. 5, 1629–1639, 2024.

[2] Tao, J., W. Zhao, X. Zhou, J. Zhang, Y. Zhang, M. Fan, M. Wu, L. Liu, Z. Zhou, H. Zhu, and J. Xiong, "Robust all-fabric e-skin with high-temperature and corrosion tolerance for self-powered tactile sensing," *Nano Energy*, Vol. 128, 109930, 2024.

[3] Zhang, S., Z. Xiong, B. Ji, N. Li, Z. Yu, S. Wu, and S. He, "Water pipeline leakage detection based on coherent φ-OTDR and deep learning technology," *Applied Sciences*, Vol. 14, No. 9, 3814, 2024.

[4] Wu, X., S. Wu, X. Chen, H. Lin, E. Forsberg, and S. He, "An ultra-compact and reproducible fiber tip michelson interferometer for high-temperature sensing," *Progress In Electromagnetics Research*, Vol. 172, 89–99, 2021.

[5] He, Z. and Q. Liu, "Optical fiber distributed acoustic sensors: A review," *Journal of Lightwave Technology*, Vol. 39, No. 12, 3671–3686, 2021.

[6] Lu, P., N. Lalam, M. Badar, B. Liu, B. T. Chorpening, M. P. Buric, and P. R. Ohodnicki, "Distributed optical fiber sensing: Review and perspective," *Applied Physics Reviews*, Vol. 6, No. 4, 041302, 2019.

[7] Sinha, S. K., J. Yang, Y. Yang, A. Nigh, and K. Soga, "Thermal response test of geothermal boreholes using distributed fiber optic sensing," in *Geo-Congress 2024*, 493–503, 2024.

[8] Dvoynikov, M. V. and P. A. Kutuzov, "Analysis of efficiency of communication channels for monitoring and operational control of oil and gas wells drilling process," *International Journal of Engineering, Transactions A: Basics*, Vol. 38, No. 1, 120–131, 2025.

[9] Ghazali, M. F., H. Mohamad, M. Y. M. Nasir, A. Hamzh, M. A. Abdullah, N. F. A. Aziz, P. Thansirichaisree, and M. S. D. Zan, "State-of-the-art application and challenges of optical fibre distributed acoustic sensing in civil engineering," *Optical Fiber Technology*, Vol. 87, 103911, 2024.

[10] Xu, L., Z. Wen, H. Su, S. Cola, N. Fabbian, Y. Feng, and S. Yang, "An innovative method integrating two deep learning networks and hyperparameter optimization for identifying fiber optic temperature measurements in earth-rock dams," *Advances in Engineering Software*, Vol. 199, 103802, 2025.

[11] Zhai, Q., A. Husker, Z. Zhan, E. Biondi, J. Yin, F. Civilini, and L. Costa, "Assessing the feasibility of Distributed Acoustic Sensing (DAS) for moonquake detection," *Earth and Planetary Science Letters*, Vol. 635, 118695, 2024.

[12] Zheng, Z., H. Feng, Z. Sha, and Z. Zeng, "A hand-crafted φ-OTDR event recognition method based on space-temporal graph and morphological object detection," *Optics and Lasers in Engineering*, Vol. 183, 108513, 2024.

[13] Chaube, P., B. G. Colpitts, D. Jagannathan, and A. W. Brown, "Distributed fiber-optic sensor for dynamic strain measurement," *IEEE Sensors Journal*, Vol. 8, No. 7, 1067–1072, 2008.

[14] He, H., Z. Zhao, S. Fu, D. Liu, and M. Tang, "High spatial resolution fast brillouin optical time-domain analysis enabled by frequency-agility digital optical frequency comb," *Optics Letters*, Vol. 47, No. 14, 3403–3406, 2022.

[15] Voskoboinik, A., A. E. Willner, and M. Tur, "Extending the dynamic range of sweep-free brillouin optical time-domain analyzer," *Journal of Lightwave Technology*, Vol. 33, No. 14, 2978–2985, 2015.

[16] Zhou, D., Y. Dong, B. Wang, C. Pang, D. Ba, H. Zhang, Z. Lu, H. Li, and X. Bao, "Single-shot BOTDA based on an optical chirp chain probe wave for distributed ultrafast measurement," *Light: Science & Applications*, Vol. 7, No. 1, 32, 2018.

[17] Wang, B., B. Fan, D. Zhou, C. Pang, Y. Li, D. Ba, and Y. Dong, "High-performance optical chirp chain BOTDA by using a pattern recognition algorithm and the differential pulse-width pair technique," *Photonics Research*, Vol. 7, No. 6, 652–658, 2019.

[18] Wang, Y., L. Chen, and X. Bao, "Single-shot chirped pulse BOTDA for static and dynamic strain sensing," *Optics Letters*, Vol. 46, No. 22, 5774–5777, 2021.

[19] Ba, D., B. Wang, D. Zhou, M. Yin, Y. Dong, H. Li, Z. Lu, and Z. Fan, "Distributed measurement of dynamic strain based on multi-slope assisted fast BOTDA," *Optics Express*, Vol. 24, No. 9, 9781–9793, 2016.

[20] Urricelqui, J., A. Zornoza, M. Sagues, and A. Loayssa, "Dynamic BOTDA measurements using Brillouin phase-shift," in *OFS2012 22nd International Conference on Optical Fiber Sensors*, Vol. 8421, 402–405, 2012.

[21] Motil, A., O. Danon, Y. Peled, and M. Tur, "Pump-power-independent double slope-assisted distributed and fast brillouin fiber-optic sensor," *IEEE Photonics Technology Letters*, Vol. 26, No. 8, 797–800, Apr. 2014.

[22] Mariñelarena, J., J. Urricelqui, and A. Loayssa, "Enhancement of the dynamic range in slope-assisted coherent Brillouin optical time-domain analysis sensors," *IEEE Photonics Journal*, Vol. 9, No. 3, 1–10, 2017.

[23] Hoshino, K., D. Saito, Y. Endo, T. Hasegawa, and Y. Tanaka, "Brillouin gain spectrum manipulation using multifrequency pump and probe for slope-assisted BOTDA with wider dynamic range," *Applied Physics Express*, Vol. 15, No. 2, 022009, 2022.

[24] Yang, G., X. Fan, B. Wang, and Z. He, "Enhancing strain dynamic range of slope-assisted BOTDA by manipulating Brillouin gain spectrum shape," *Optics Express*, Vol. 26, No. 25, 32 599–32 607, 2018.

[25] Yang, G., X. Fan, and Z. He, "Strain dynamic range enlargement of slope-assisted BOTDA by using Brillouin phase-gain ratio," *Journal of Lightwave Technology*, Vol. 35, No. 20, 4451–4458, Oct. 2017.

[26] Zhou, D., Y. Dong, B. Wang, T. Jiang, D. Ba, P. Xu, H. Zhang, Z. Lu, and H. Li, "Slope-assisted BOTDA based on vector SBS and frequency-agile technique for wide-strain-range dynamic measurements," *Optics Express*, Vol. 25, No. 3, 1889–1902, 2017.

[27] Zheng, H., D. Feng, J. Zhang, T. Zhu, Y. Bai, D. Qu, X. Huang, and F. Qiu, "Distributed vibration measurement based on a coherent multi-slope-assisted BOTDA with a large dynamic range," *Optics Letters*, Vol. 44, No. 5, 1245–1248, 2019.

[28] Urricelqui, J., F. López-Fernandino, M. Sagues, and A. Loayssa, "Polarization diversity scheme for BOTDA sensors based on a double orthogonal pump interaction," *Journal of Lightwave Technology*, Vol. 33, No. 12, 2633–2638, Jun. 2015.

[29] Bernini, R., A. Minardo, and L. Zeni, "Dynamic strain measurement in optical fibers by stimulated Brillouin scattering," *Optics Letters*, Vol. 34, No. 17, 2613–2615, 2009.

[30] Peled, Y., A. Motil, L. Yaron, and M. Tur, "Slope-assisted fast distributed sensing in optical fibers with arbitrary brillouin profile," *Optics Express*, Vol. 19, No. 21, 19 845–19 854, Oct. 2011.